Dual-energy computed tomography to assess intra- and inter-patient tissue variability for proton treatment planning of brain-tumor patients

Wohlfahrt, P.; Möhler, C.; Troost, E.; Greilich, S.; Richter, C.;

Originally published:

July 2019

Radiotherapy and Oncology 105(2019)3, 504-513

DOI: https://doi.org/10.1016/j.ijrobp.2019.06.2529

Perma-Link to Publication Repository of HZDR:

https://www.hzdr.de/publications/Publ-27917

TITLE: Dual-energy computed tomography to assess intra- and inter-patient tissue variability for proton treatment planning of brain-tumor patients

SHORTENED RUNNING TITLE: DECT-based tissue variability assessment

Authors: Patrick Wohlfahrt[*,†], Christian Möhler[‡,§], Esther G. C. Troost[*,†,‖,¶,#], Steffen Greilich[‡,§], Christian Richter[*,†,‖,¶]

Institutions:

[*] OncoRay - National Center for Radiation Research in Oncology, Faculty of Medicine and University Hospital Carl Gustav Carus, Technische Universität Dresden, Helmholtz-Zentrum Dresden - Rossendorf, Dresden, Germany

[†] Helmholtz-Zentrum Dresden - Rossendorf, Institute of Radiooncology - OncoRay, Dresden, Germany

[‡] German Cancer Research Center (DKFZ), Heidelberg, Germany

[§] National Center for Radiation Research in Oncology (NCRO), Heidelberg Institute for Radiation Oncology (HIRO), Heidelberg, Germany

[‖] Department of Radiotherapy and Radiation Oncology, Faculty of Medicine and University Hospital Carl Gustav Carus, Technische Universität Dresden, Dresden, Germany

[¶] German Cancer Consortium (DKTK), Partner Site Dresden, Germany

[#] National Center for Tumor Diseases (NCT), Partner Site Dresden, Germany: German Cancer Research Center (DKFZ), Heidelberg, Germany; Faculty of Medicine and University Hospital Carl Gustav Carus, Technische Universität Dresden, Dresden, Germany, and; Helmholtz Association / Helmholtz-Zentrum Dresden - Rossendorf, Dresden, Germany

Corresponding author: Patrick Wohlfahrt, PhD, OncoRay - National Center for Radiation Research in Oncology, Faculty of Medicine and University Hospital Carl Gustav Carus, Technische Universität Dresden, Helmholtz-Zentrum Dresden - Rossendorf, Dresden, Germany, Tel. +49 351 458 7626, E-mail: Patrick.Wohlfahrt@OncoRay.de

Keywords: dual-energy CT; tissue variability; proton therapy

Total number of pages: 26

Number of tables: 0

Number of figures: 6

ABSTRACT:

Background and Purpose:

Range prediction in particle therapy is associated with an uncertainty originating from the calculation of stopping-power ratio (SPR) based on x-ray computed tomography (CT). Here, we assessed the intra- and inter-patient variability of tissue properties in primary brain-tumor patients using dual-energy CT (DECT) and quantified its influence on current SPR prediction.

Material and Methods:

Based on 102 patient DECT scans, SPR distributions were derived from a patient-specific DECT-based approach. Tissue-specific and global deviations between this method and the state-of-the-art CT-number-to-SPR conversion applying a Hounsfield look-up table (HLUT) were quantified. To isolate systematic deviations between both, the HLUT was optimized using DECT. Subsequently, the influence of soft tissue diversity and age-related variations in bone composition on SPR were assessed.

Results:

An intra-patient ± inter-patient soft tissue diversity of (4.4±0.7)% in SPR was obtained after conservative consideration of noise-induced variation. Between adults and children younger than 6 years, age-related variations in bone composition resulted in a median SPR difference of approximately 5%.

Conclusions:

Patient-specific DECT-based stopping-power prediction can intrinsically incorporate most of the SPR variability arising from tissue mixtures, inter-patient and intra-tissue variations. Since the state-of-the-art HLUT - even after cohort-specific optimization - cannot fully consider the

broad tissue variability, patient-specific DECT-based stopping-power prediction is advisable in particle therapy.

MANUSCRIPT:

Introduction

To facilitate accurate and high-conformal radiation treatment planning, a reliable determination of the individual tissue compositions of each patient is worthwhile [1]. Especially in proton and ion-beam therapy, a precise range prediction from x-ray computed tomography (CT) is essential to translate the particle beam's physical advantage into a further improved clinical outcome [2–4].

The current acquisition of single-energy CT scans and their conversion from CT number to stopping-power ratio (SPR) using a generic Hounsfield look-up table (HLUT) are restricted to specific material compositions and cannot adequately account for tissue diversity [5,6]. The associated CT-related uncertainty of range calculation is covered by considerable safety margins added in beam direction or is incorporated in robust optimization techniques leading to an increased dose to healthy tissue, which is worth to be reduced [7–10]. Since there are substantial intra- and inter-patient variations in elemental composition of human tissues [5], appropriate and adequately commissioned imaging techniques are desirable to accurately quantify the respective tissue distribution and variability.

With the advent of clinical dual-energy CT (DECT) scanners in radiology and radiotherapy, additional tissue information can be obtained from two CT scans of different x-ray spectra allowing for a better material differentiation compared with single-energy CT [11,12]. Hence, the clinical application of DECT for proton treatment planning [13] is expected to inherently incorporate most of intra- and inter-patient tissue variability in a patient-specific SPR prediction [14–16], since the empirical component in CT-based SPR calculation is strongly mitigated. In recently published studies, the reliability and superior accuracy of DECT-based SPR prediction as an alternative to the current state-of-the-art application of a generic HLUT were demonstrated under clinical conditions in an anthropomorphic head phantom [17] and in biological tissue samples [18–20], and finally transferred to relative range shifts obtained in

patients [21,22]. Consequently, DECT can presumably contribute to a reduction of the CT-related range uncertainty and associated safety margins.

In this study, DECT scans acquired for proton treatment planning of 102 primary brain-tumor patients were retrospectively evaluated to assess the intra- and inter-patient variability of CT-based SPR prediction originating from various tissue types, tissue mixtures and intra-tissue variations.

Material and Methods

Patient cohort and DECT imaging

In total, 102 primary brain-tumor patients (40 women, 40 men and 22 children younger than 20 years) treated with proton therapy at OncoRay (Dresden, Germany) were selected covering a wide range of brain-tumor entities (36 glioblastoma, 25 astrocytoma, 13 meningioma, 9 sarcoma, 7 adenoma, 7 glioma, 2 craniopharyngioma, 2 ependymoma and 1 germinoma) and patient age (1-80 years, median age of 45 years). This retrospective study was approved by the local ethics committee (EK535122015).

For each patient, a DECT scan (80/140 kVp) with $1\times1\times2$ mm^3 voxel spacing and $CTDIvol_{32cm}$ of 20.8 mGy was acquired at a single-source CT scanner SOMATOM Definition AS (Siemens Healthineers, Forchheim, Germany) [13]. Image reconstruction was performed using the iterative reconstruction kernel Q34f/5 (SAFIRE at maximal strength), which includes a beam hardening correction for bone, to reduce image noise and patient-size dependent CT number variations. An image noise level (CT number variation expressed by ± two standard deviations) of 5 HU was determined for this scan setting in a homogeneous brain region of an anthropomorphic head phantom (Proton Therapy Dosimetry Head, Model 731-HN, CIRS, Inc., Norfolk, VA).

Tissue parameter extraction

The DECT scans were post-processed in the SYNGO.VIA environment (Siemens Healthineers, Forchheim, Germany) to calculate 79 keV pseudo-monoenergetic CT (MonoCT), 170 keV MonoCT and effective atomic number (EAN) datasets using the modules SYNGO.CT DE MONOENERGETIC PLUS and SYNGO.CT DE RHO/Z. Based on an individual CT scanner calibration [13], the relative electron density (RED) was obtained from 170 keV MonoCT datasets. Dividing 79 keV MonoCT by RED resulted in the relative photon attenuation cross section (RCS). Both quantities are then inserted in the Bethe equation [23] to directly determine the SPR (DirectSPR). This approach, referred to as RhoSigma [16], was implemented as described in [17,21]. An image noise level of 6 HU (corresponding to two standard deviations) was obtained for the calculated SPR datasets in the anthropomorphic head phantom.

To consider only voxels within the patient, an external contour was automatically created based on the 80/140 kVp DECT scan using a threshold of -500 HU. This contour, covering the patient surface, was subsequently shrunk by 3 (5) voxels in x (y) direction to exclude remaining parts of immobilization devices. In scan direction, the datasets were restricted to only include the head from chin to calvaria. Within this defined volume, the frequency distribution of voxelwise correlations of two tissue parameters were determined, i.e., SPR and RED depending on CT number H as well as EAN and RCS depending on RED as shown in Figure 1.

The intra- and inter-patient variability was quantified based on the frequency distribution of (H, SPR) correlations to assess the degree of non-uniqueness of a heuristic CT-number-to-SPR conversion. The diversity of human soft tissues due to tissue mixtures and different tissue types was characterized by the frequency-weighted average spread ω in SPR covering 95% of all CT voxels within the soft-tissue region ($-125\ \text{HU} \leq H \leq 75\ \text{HU}$):

$$\omega = \frac{1}{N_{\mathrm{Total}}} \sum_{H} N(H) \cdot \left[p_{97.5,\,\mathrm{SPR}}(H) - p_{2.5,\,\mathrm{SPR}}(H) \right] \quad (1)$$

with N_{Total} as total number of voxels, $N(H)$ as number of voxels with respective CT number, $p_{x,SPR}$ as xth SPR percentile.

Within the bony region ($100\ \mathrm{HU} \leq H \leq 1800\ \mathrm{HU}$), the variation of slope α of an intensity-weighted linear regression within the (H, SPR) domain serves as measure for variations in human bones.

Significant variations between adults and children were assessed by two-sample t-tests with significance criterion of 5%.

Compensation of systematic deviations in stopping-power prediction

As previously demonstrated for brain-tumor patients, CT-based SPR prediction significantly differs between the application of an HLUT and a DECT-based DirectSPR method [21]. This results in a systematic global SPR and range deviation, which is very likely caused by tissue compositions and tissue distributions differing from HLUT calibration conditions [24]. Hence, the SPR difference between the HLUT and DirectSPR approach is influenced by a combination of this systematic deviation as well as the intra- and inter-patient variability reflecting the ambiguity of the heuristic CT-number-to-SPR conversion. To isolate the influence of tissue variability on SPR prediction, the HLUT was adapted by minimizing the systematic deviation between both methods. For this purpose, the median SPR of each CT number was obtained from the frequency distribution of (H, SPR) correlations. Subsequently, the Hounsfield scale was divided in four classes corresponding to various tissue types: low-density ($-950\ \mathrm{HU} \leq H \leq -160\ \mathrm{HU}$), adipose ($-140\ \mathrm{HU} \leq H \leq -40\ \mathrm{HU}$), muscle and brain ($-20\ \mathrm{HU} \leq H \leq 40\ \mathrm{HU}$) as well as bone tissue ($100\ \mathrm{HU} \leq H \leq 1800\ \mathrm{HU}$). For each tissue class, the median SPR distribution was described by an intensity-weighted linear regression depending on the relative occurrence of the respective CT number within the patients. The

transitions between different classes were linearly connected, which finally resulted in the cohort-specifically adapted HLUT.

Assessment of SPR and range deviations

The mean signed and absolute SPR deviation between both CT-based SPR prediction approaches ($SPR_{HLUT} - SPR_{RhoSigma}$) was calculated including all CT voxels within the patient's external contour. Tissue-dependent SPR differences were quantified using only CT voxels of the respective tissue class as defined above.

To check whether the findings obtained on SPR level could be transferred to range deviations, passively scattered proton treatment plans of two representative patients were recalculated on SPR datasets derived from RhoSigma, clinical and adapted HLUT using XIO (Elekta AB, Stockholm, Sweden) with a 1×1×1 mm^3 dose calculation grid. The distal range at 80% of prescribed dose was determined for more than 5000 line-dose profiles in beam direction to assess proton range shifts.

Results

Tissue occurence

The investigated body region (head) mainly contains soft tissues (adipose, brain and muscles) and bones with a mean fraction ± one standard deviation between different patients of $(78.6 \pm 2.5)\%$ and $(18.9 \pm 2.3)\%$, respectively. The remaining, small fraction of apparent low-density tissue of $(2.5\% \pm 0.5\%)$ is mostly caused by a sub-voxel mixture of air cavities and various soft tissues or even bones.

Soft tissue diversity

As illustrated in Figure 1, children and adults showed a similar soft tissue distribution in all physical quantities studied. The soft tissue region is dominated by brain ($H \approx 40$HU, $RED \approx$

1.034) and adipose tissue ($H \approx -100\text{HU}$, $RED \approx 0.920$). Even though, a broad SPR distribution with a mean intra-patient SPR spread ± one standard deviation of $\omega = (5.6 \pm 0.7)\%$ was found. This was induced by various tissue types, intra-tissue variations and mixtures between brain and adipose tissue (indicated by a clearly visible line between the tissue peaks) as well as between soft and low-density or bone tissues. The intra-patient SPR spread within the soft tissue region differed significantly between children and adults ($p \ll 0.001$, Figure 2). The increased soft tissue diversity in adults may potentially arise from the large intrinsic variability within adipose tissues, e.g. the varying relative amount of lipids from 61.4% to 87.3% [5], in combination with a slightly higher mean relative amount of adipose tissue in adults $(16.5 \pm 4.0)\%$ compared to children $(12.7 \pm 4.0)\%$ (cf., equation 1).

Variations in bone composition

The distribution of bones differed between adults and children as indicated by a linear fit for $\text{SPR}(H)$ and $\text{RED}(H)$ and power-function fit for $\text{EAN}(\text{RED})$ and $\text{RCS}(\text{RED})$ in Figure 1. Bones in children revealed a smaller effective atomic number at same electron density and an age-related significant reduction of the slope within the $\text{SPR}(H)$ domain (Figure 2), which are presumably associated with a smaller relative amount of calcium embedded [5,25]. Since the calcium content in bones increases with age, the influence of the photoelectric effect on CT number also increases.

Compensation of systematic SPR deviations

To reduce systematic deviations in CT-number-to-SPR conversion, the HLUT was optimized based on the DECT-derived SPR (Figure 3). The HLUT refinement was performed separately for each patient cohort considering the difference in bone composition (Figure 2). The SPR differences before (Figure 4A) and after HLUT adaptation (Figure 4B) for adults and children demonstrated that a HLUT refinement can effectively compensate systematic deviations in

stopping-power prediction between the RhoSigma and HLUT approach. The HLUT adaptation resulted in a significant reduction of systematic SPR deviations ± one standard deviation from $(2.0 \pm 0.6)\%$ to $(0.1 \pm 0.6)\%$ for low-density tissues, $(1.9 \pm 0.2)\%$ to $(0.1 \pm 0.2)\%$ for soft tissues, $(-2.4 \pm 0.9)\%$ to $(-0.3 \pm 0.7)\%$ for bones and $(1.1 \pm 0.3)\%$ to $(0.0 \pm 0.3)\%$ in total considering all 102 patients (Figure 5A).

Residual intra- and inter-patient SPR variability

After removing systematic deviations between the HLUT and RhoSigma approach, the residual SPR deviations between both methods were assessed. The intra-patient SPR deviations of a representative child and adult were comparable to SPR differences including all patients within the respective cohort (Figure 4). The SPR variability within one patient (e.g., $\omega = 5.6\%$ for soft tissues) is considerably larger than the variability between patients (e.g., one standard deviation of ω is 0.7% for soft tissues). The broad distribution of SPR deviations within adipose tissue (Figure 4) results in SPR differences up to 10% (relative to the SPR of water), considering (H, SPR) correlations with a relative amount larger than 0.01‰, and leads to a mean intra-patient SPR spread ± one standard deviation of $\omega = (9.8 \pm 1.2)\%$ for adipose tissues only.

Despite the HLUT refinement, the intra-patient SPR variation remained almost unchanged in soft tissues (Figure 4B). SPR variations in a single patient after (before) HLUT adaptation translated into mean absolute SPR deviations of approximately 3% (4%) for low-density tissues, 3% (6%) for bones as well as 1% (2%) for soft tissues. The latter corresponds to the mean intra-patient SPR spread of $\omega = 5.6\%$ within soft tissues (Figure 5B). The large inter-patient variation of SPR deviations in bones (Figure 5, interquartile range) illustrated the high variability in bone composition between patients.

Discussion

The evaluation of DECT scans of 102 primary brain-tumor patients revealed a considerable intra-patient soft tissue diversity leading to a broad SPR distribution with a frequency-weighted average spread of $\omega = (5.6 \pm 0.7)\%$. However, this SPR spread does not only stem from different tissue types, tissue mixtures and intra-tissue variability, but also from image noise. The influence of image noise on SPR prediction was minimized by applying an iterative image reconstruction algorithm at maximal strength. It was estimated as 1.2% (relative to the SPR of water), which equals twice the image noise level (± two standard deviations) of 6 HU in the calculated SPR dataset. This results in a noise-corrected mean SPR spread of $\omega = 5.5\%$ (4.4%) using quadratic (linear) subtraction. This intra-patient SPR variability in the soft tissue region is associated with a mean absolute SPR deviation between the RhoSigma and HLUT approach of 1.2% (cf., Figure 5).

Furthermore, differences in bone composition between adults and children were observed. An HLUT specified for adults would cause a SPR underestimation in bone of approximately 5% for children younger than 6 years. To further validate the detected age-related changes in bone composition, the investigated pediatric patient cohort may be extended in follow-up studies allowing for a better age resolution. Additional studies may also analyze whether DECT can further improve the quantification of senile osteoporosis in patients [26,27].

A refinement of the HLUT based on DECT-derived tissue information can on average reduce the systematic global and tissue-specific SPR deviations between both CT-number-to-SPR conversion methods. These systematic deviations originate from different tissue compositions and distributions in patients as compared to the tissue surrogates used for HLUT specification [24]. As exemplarily shown in Figure 6 for a representative child and adult, the mean relative range deviation between RhoSigma and HLUT can also be reduced by applying the adapted HLUT (Figure 6). However, depending on the tissues traversed in beam direction, CT-based SPR prediction using either the adapted HLUT or RhoSigma can still result in range

differences of about 1% as illustrated by the standard deviation of the obtained range shifts (Figure 6). The HLUT adaptation presented in this study was only based on the tissue diversity within brain-tumor patients. In a further study, we are going to rather focus on the irradiated volume of each patient including also immobilization devices. In addition, we also consider patients with tumors located in other body regions such as thorax or pelvis to comprehensively evaluate their influence on a HLUT refinement.

Within this study, the integral intra- and inter-patient variability of tissue properties were determined in primary brain-tumor patients without distinguishing different organs or anatomical structures. Further evaluations could individually assess the variability of specific tissue types to update or supplement already existing patient tissue databases [5,25]. Moreover, the intra- and inter-patient variability of other body regions is to be evaluated (e.g., thorax and pelvis) to assess potential differences in tissue composition and distribution.

Conclusions

The presented investigation of the intra- and inter-patient SPR variability, as assessed in 102 primary brain-tumor patients using dual-energy CT for the first time, highlights a general limitation of the state-of-the-art HLUT approach. The age-related bone variation (inter-patient SPR deviations of roughly 5% between young children and adults) and the considerable soft tissue variability in general (mean intra-patient SPR spread of 4-6% for a defined CT number) cannot be fully accounted for by a generic HLUT. This leads to unavoidable deviations in SPR prediction. The resulting contribution on SPR accuracy was so far only partly considered in the uncertainty estimation of the HLUT approach and demonstrates a further advantage of a DECT-based DirectSPR approach. Hence, an accurate patient-specific SPR prediction using dual-energy CT is advisable for particle treatment planning, since it correctly handles tissue mixtures and intrinsically incorporates most of intra- and inter-patient variability.

Acknowledgments:

This work was funded by the National Center for Radiation Oncology (NCRO) within the project “Translation of dual-energy CT into application in particle therapy”.

Conflict of Interest Statement: The authors report no conflict of interest. OncoRay and DKFZ have institutional research agreements with Siemens Healthineers.

REFERENCES

[1] Baumann M, Krause M, Overgaard J, Debus J, Bentzen SM, Daartz J, et al. Radiation Oncology in the Era of Precision Medicine. Nat Rev Cancer 2016;16:234–49. doi:10.1038/nrc.2016.18.

[2] Paganetti H. Range Uncertainties in Proton Therapy and the Role of Monte Carlo Simulations. Phys Med Biol 2012;57:R99–117. doi:10.1088/0031-9155/57/11/R99.

[3] Knopf A-C, Lomax AJ. In vivo proton range verification: a review. Phys Med Biol 2013;58:R131–60. doi:10.1088/0031-9155/58/15/R131.

[4] Dinges E, Felderman N, McGuire S, Gross B, Bhatia S, Mott S, et al. Bone marrow sparing in intensity modulated proton therapy for cervical cancer: Efficacy and robustness under range and setup uncertainties. Radiother Oncol 2015;115:373–8. doi:10.1016/j.radonc.2015.05.005.

[5] Woodard HQ, White DR. The Composition of Body Tissues. Br J Radiol 1986;59:1209–19. doi:10.1259/0007-1285-59-708-1209.

[6] Yang M, Virshup G, Clayton J, Zhu XR, Mohan R, Dong L. Theoretical Variance Analysis of Single- and Dual-Energy Computed Tomography Methods for Calculating Proton Stopping Power Ratios of Biological Tissues. Phys Med Biol 2010;55:1343–62. doi:10.1088/0031-9155/55/5/006.

[7] Fattori G, Riboldi M, Scifoni E, Krämer M, Pella A, Durante M, et al. Dosimetric effects of residual uncertainties in carbon ion treatment of head chordoma. Radiother Oncol 2014;113:66–71. doi:10.1016/j.radonc.2014.08.001.

[8] Li H, Zhang X, Park P, Liu W, Chang J, Liao Z, et al. Robust Optimization in Intensity-Modulated Proton Therapy to Account for Anatomy Changes in Lung Cancer Patients. Radiother Oncol 2015;114:367–72. doi:10.1016/j.radonc.2015.01.017.

[9] Van Der Voort S, Van De Water S, Perkó Z, Heijmen B, Lathouwers D, Hoogeman M. Robustness Recipes for Minimax Robust Optimization in Intensity Modulated Proton

Therapy for Oropharyngeal Cancer Patients. Int J Radiat Oncol Biol Phys 2016;95:163–70. doi:10.1016/j.ijrobp.2016.02.035.

[10] Stützer K, Lin A, Kirk M, Lin L. Superiority in Robustness of Multifield Optimization Over Single-Field Optimization for Pencil-Beam Proton Therapy for Oropharynx Carcinoma: An Enhanced Robustness Analysis. Int J Radiat Oncol Biol Phys 2017;99:738–49. doi:10.1016/j.ijrobp.2017.06.017.

[11] Flohr TG, McCollough CH, Bruder H, Petersilka M, Gruber K, Süß C, et al. First Performance Evaluation of a Dual-Source CT (DSCT) System. Eur Radiol 2006;16:256–68. doi:10.1007/s00330-005-2919-2.

[12] van Elmpt W, Landry G, Das M, Verhaegen F. Dual Energy CT in Radiotherapy: Current Applications and Future Outlook. Radiother Oncol 2016;119:137–44. doi:10.1016/j.radonc.2016.02.026.

[13] Wohlfahrt P, Möhler C, Hietschold V, Menkel S, Greilich S, Krause M, et al. Clinical Implementation of Dual-Energy CT for Proton Treatment Planning on Pseudo-Monoenergetic CT Scans. Int J Radiat Oncol Biol Phys 2017;97:427–34. doi:10.1016/j.ijrobp.2016.10.022.

[14] Hünemohr N, Krauss B, Tremmel C, Ackermann B, Jäkel O, Greilich S. Experimental Verification of Ion Stopping Power Prediction from Dual Energy CT Data in Tissue Surrogates. Phys Med Biol 2014;59:83–96. doi:10.1088/0031-9155/59/1/83.

[15] Bourque AE, Carrier J-F, Bouchard H. A Stoichiometric Calibration Method for Dual Energy Computed Tomography. Phys Med Biol 2014;59:2059–88. doi:10.1088/0031-9155/59/8/2059.

[16] Möhler C, Wohlfahrt P, Richter C, Greilich S. Range Prediction for Tissue Mixtures Based on Dual-Energy CT. Phys Med Biol 2016;61:N268–75. doi:10.1088/0031-9155/61/11/N268.

[17] Wohlfahrt P, Möhler C, Richter C, Greilich S. Evaluation of Stopping-Power

Prediction by Dual- and Single-Energy Computed Tomography in an Anthropomorphic Ground-Truth Phantom. Int J Radiat Oncol Biol Phys 2018;100:244–53. doi:10.1016/j.ijrobp.2017.09.025.

[18] Taasti VT, Michalak GJ, Hansen DC, Deisher AJ, Kruse JJ, Krauss B, et al. Validation of proton stopping power ratio estimation based on dual energy CT using fresh tissue samples. Phys Med Biol 2017;63:015012. doi:10.1088/1361-6560/aa952f.

[19] Bär E, Lalonde A, Zhang R, Jee K-W, Yang K, Sharp G, et al. Experimental validation of two dual-energy CT methods for proton therapy using heterogeneous tissue samples. Med Phys 2017. doi:10.1002/mp.12666.

[20] Möhler C, Russ T, Wohlfahrt P, Elter A, Runz A, Richter C, et al. Experimental Verification of Stopping-Power Prediction from Single- and Dual-Energy Computed Tomography in Biological Tissues. Phys Med Biol 2018;63:025001. doi:10.1088/1361-6560/aaa1c9.

[21] Wohlfahrt P, Möhler C, Stützer K, Greilich S, Richter C. Dual-Energy CT Based Proton Range Prediction in Head and Pelvic Tumor Patients. Radiother Oncol 2017;125:526–33. doi:10.1016/j.radonc.2017.09.042.

[22] Wohlfahrt P, Troost EGC, Hofmann C, Richter C, Jakobi A. Clinical Feasibility of Single-Source Dual-Spiral 4D Dual-Energy CT for Proton Treatment Planning Within the Thoracic Region. Int J Radiat Oncol Biol Phys 2018. doi:10.1016/j.ijrobp.2018.06.044.

[23] Bethe H. Zur Theorie des Durchgangs schneller Korpuskularstrahlen durch Materie. Ann Phys 1930;397:325–400. doi:10.1002/andp.19303970303.

[24] Wohlfahrt P, Möhler C, Greilich S, Richter C. Comment on: Dosimetric Comparison of Stopping-Power Calibration with Dual-Energy CT and Single-Energy CT in Proton Therapy Treatment Planning [Med. Phys. 43(6), 2845-2854 (2016)]. Med Phys 2017;44:5533–6. doi:10.1002/mp.12418.

[25] White DR, Widdowson EM, Woodard HQ, Dickerson JWT. The Composition of Body Tissues. (II) Fetus to Young Adult. Br J Radiol 1991;64:149–59. doi:10.1259/0007-1285-64-758-149.

[26] Wichmann JL, Booz C, Wesarg S, Kafchitsas K, Bauer RW, Kerl JM, et al. Dual-Energy CT–based Phantomless in Vivo Three-dimensional Bone Mineral Density Assessment of the Lumbar Spine. Radiology 2014;271:778–84. doi:10.1148/radiol.13131952.

[27] Booz C, Hofmann PC, Sedlmair M, Flohr TG, Schmidt B, D'Angelo T, et al. Evaluation of Bone Mineral Density of the Lumbar Spine Using a Novel Phantomless Dual-Energy CT Post-Processing Algorithm in Comparison with Dual-Energy X-ray Absorptiometry. Eur Radiol Exp 2017;1:11. doi:10.1186/s41747-017-0017-2.

389 **FIGURES**

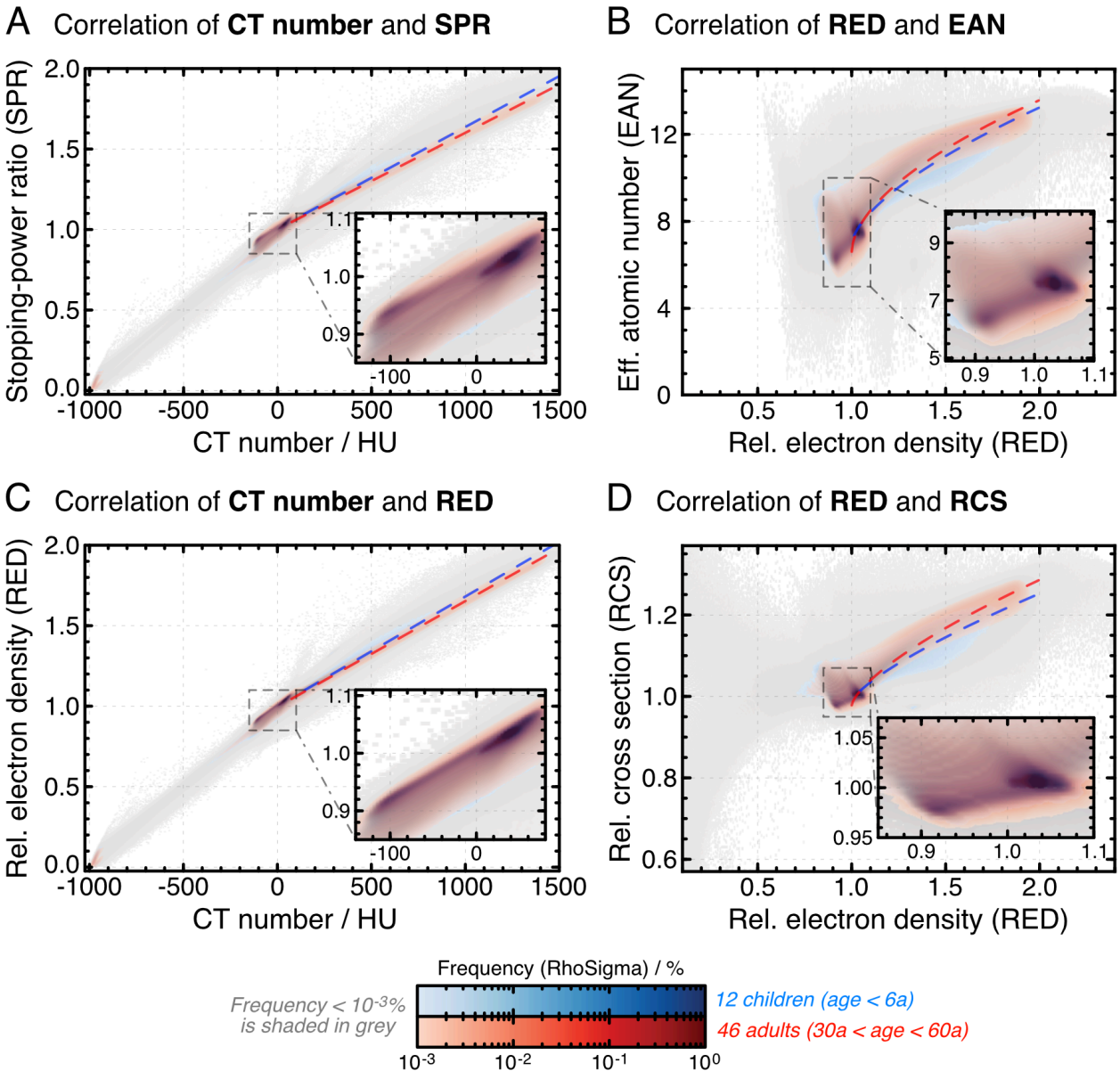

390

391 **Figure 1:** Frequency distribution of tissue parameters derived from dual-energy CT for
392 children (blue) and adults (red). The superposition of both datasets appears purple. Dashed
393 lines illustrate correlation in bony region.

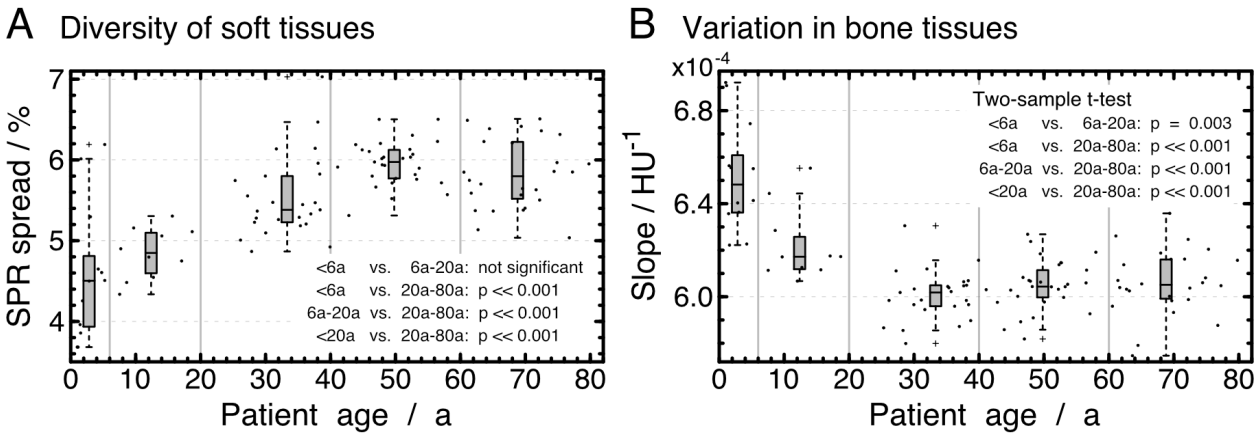

394

395 **Figure 2:** Age-related variation of (A) stopping-power ratio (SPR) spread in soft tissue (tissue
396 diversity) and (B) the slope within bones (change in calcium content) for correlations between
397 CT number and SPR. Patients were sorted in five groups depending on age (illustrated by
398 vertical lines). Boxplots are defined according to Figure 5.

399

400

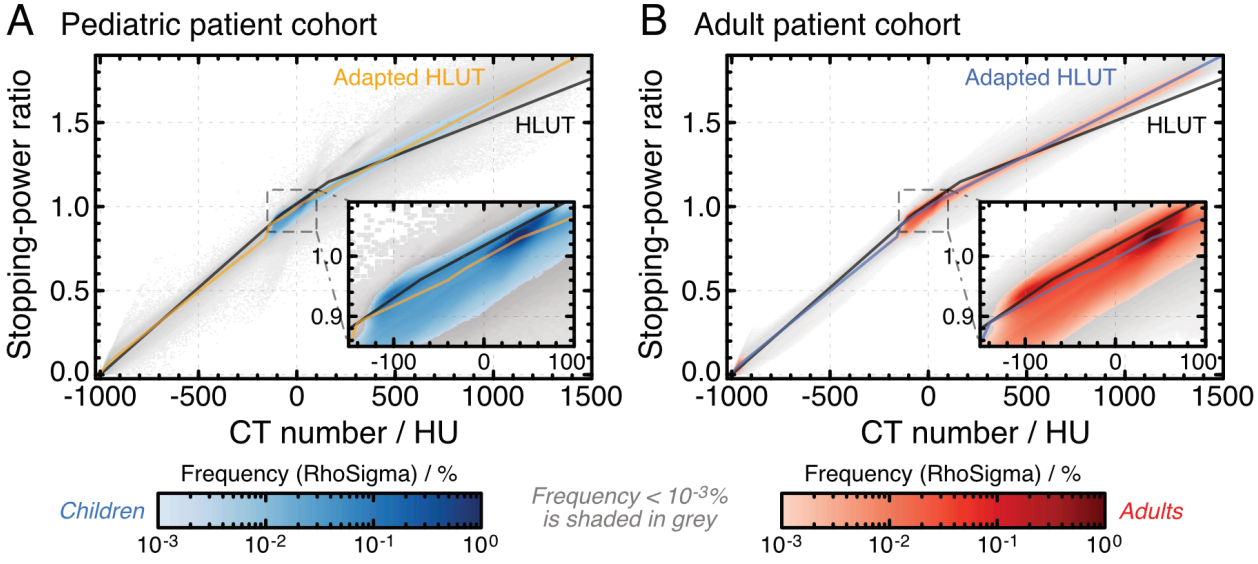

401

402 **Figure 3:** Frequency distribution of correlations between CT number and stopping-power
403 ratio (SPR) for the (A) pediatric (younger than 20 years) and (B) adult patient cohort.

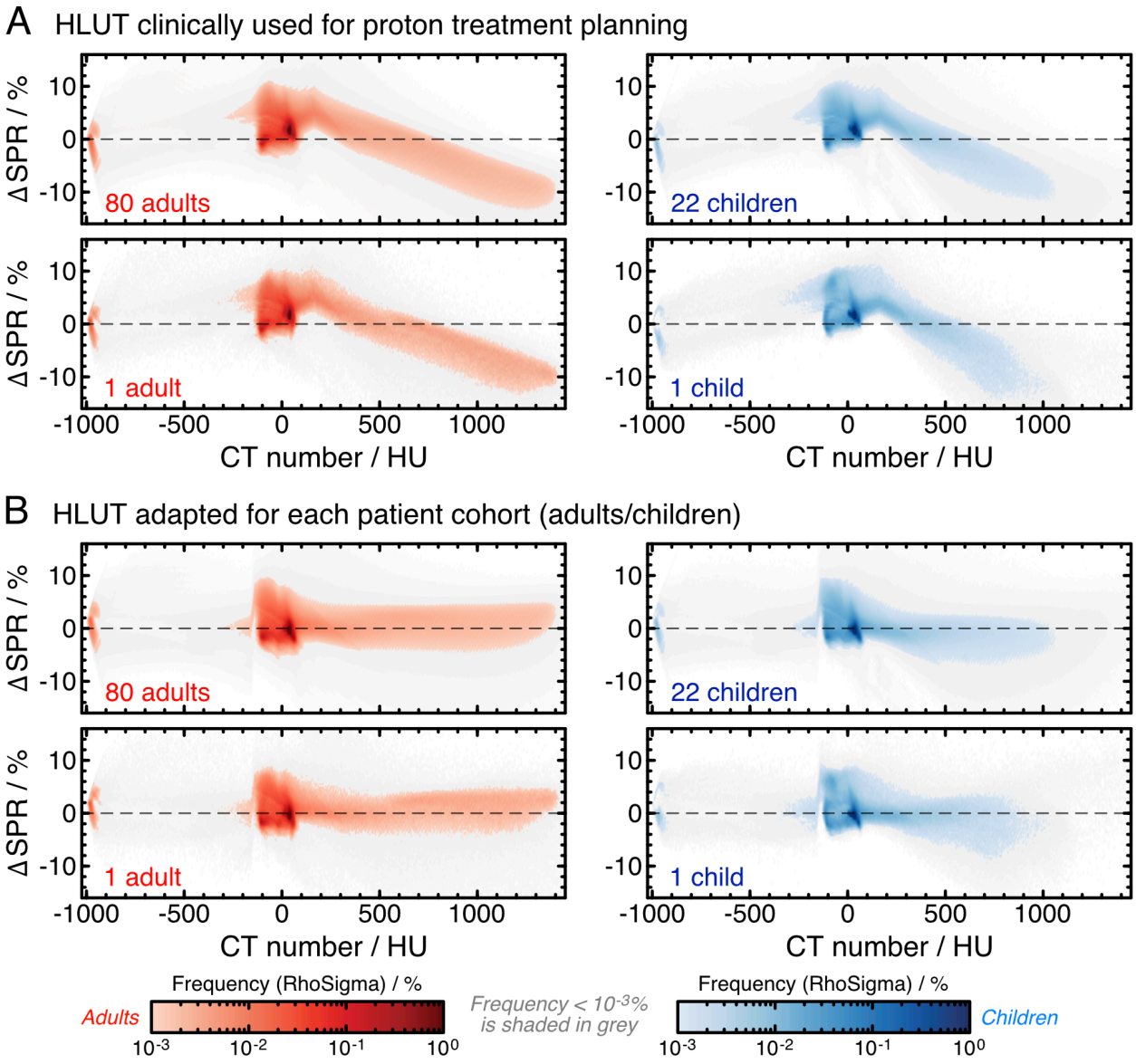

404

405 **Figure 4:** Difference in stopping-power ratio (SPR) between the dual-energy CT based SPR
406 prediction (RhoSigma) and (A) clinically applied or (B) cohort-specifically adapted
407 Hounsfield look-up table (HLUT) to visually compare the frequency distribution in one
408 patient with the entire patient cohort. The colored (grey-shaded) frequency distribution covers
409 all correlations with a frequency larger (lower) than 10^{-3}%.

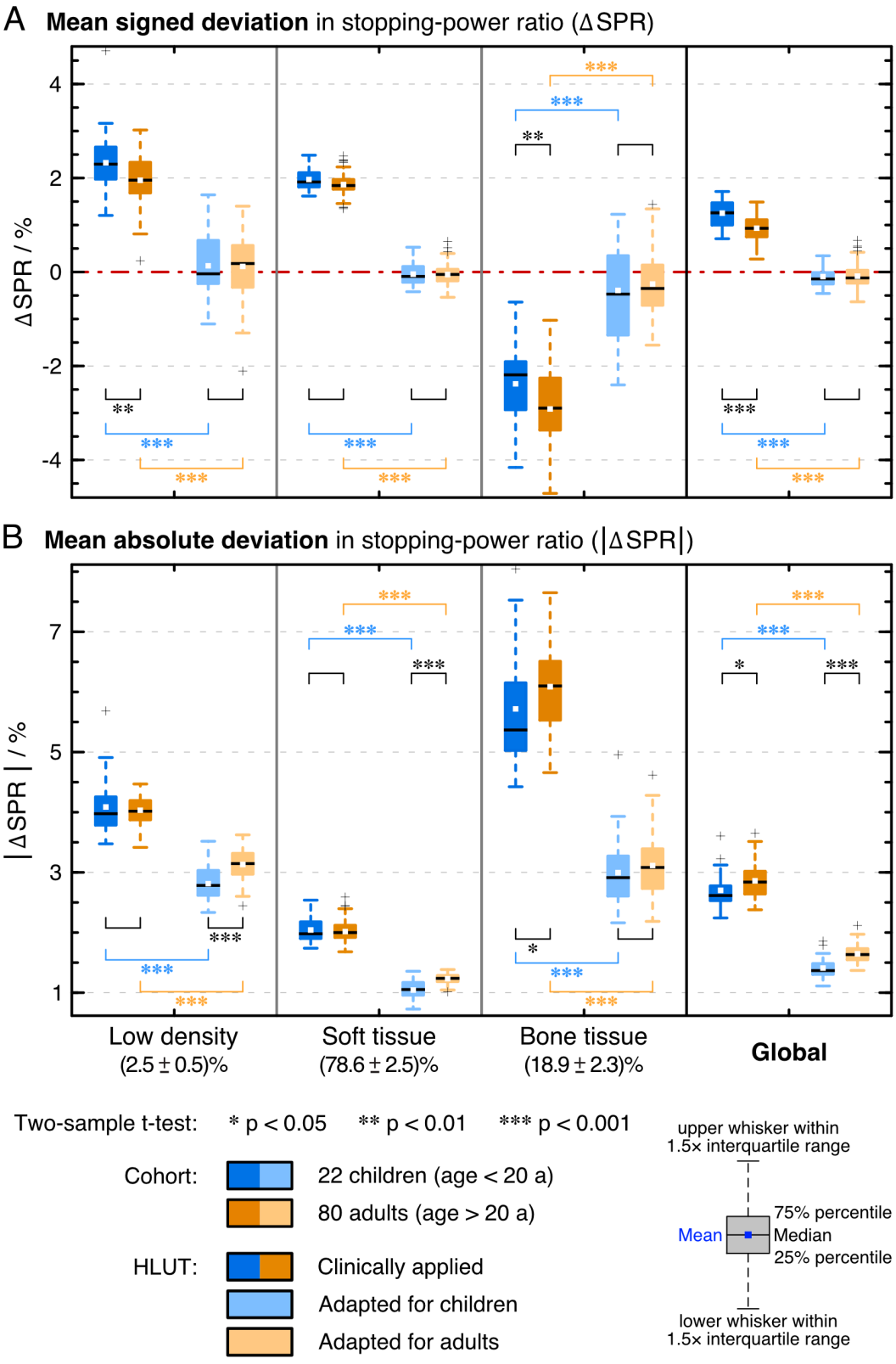

Figure 5: Global and tissue-specific mean (A) signed and (B) absolute SPR deviation between the dual-energy CT based SPR prediction and clinically applied or adapted Hounsfield look-up table (HLUT). The relative amount is quoted for each tissue type below.

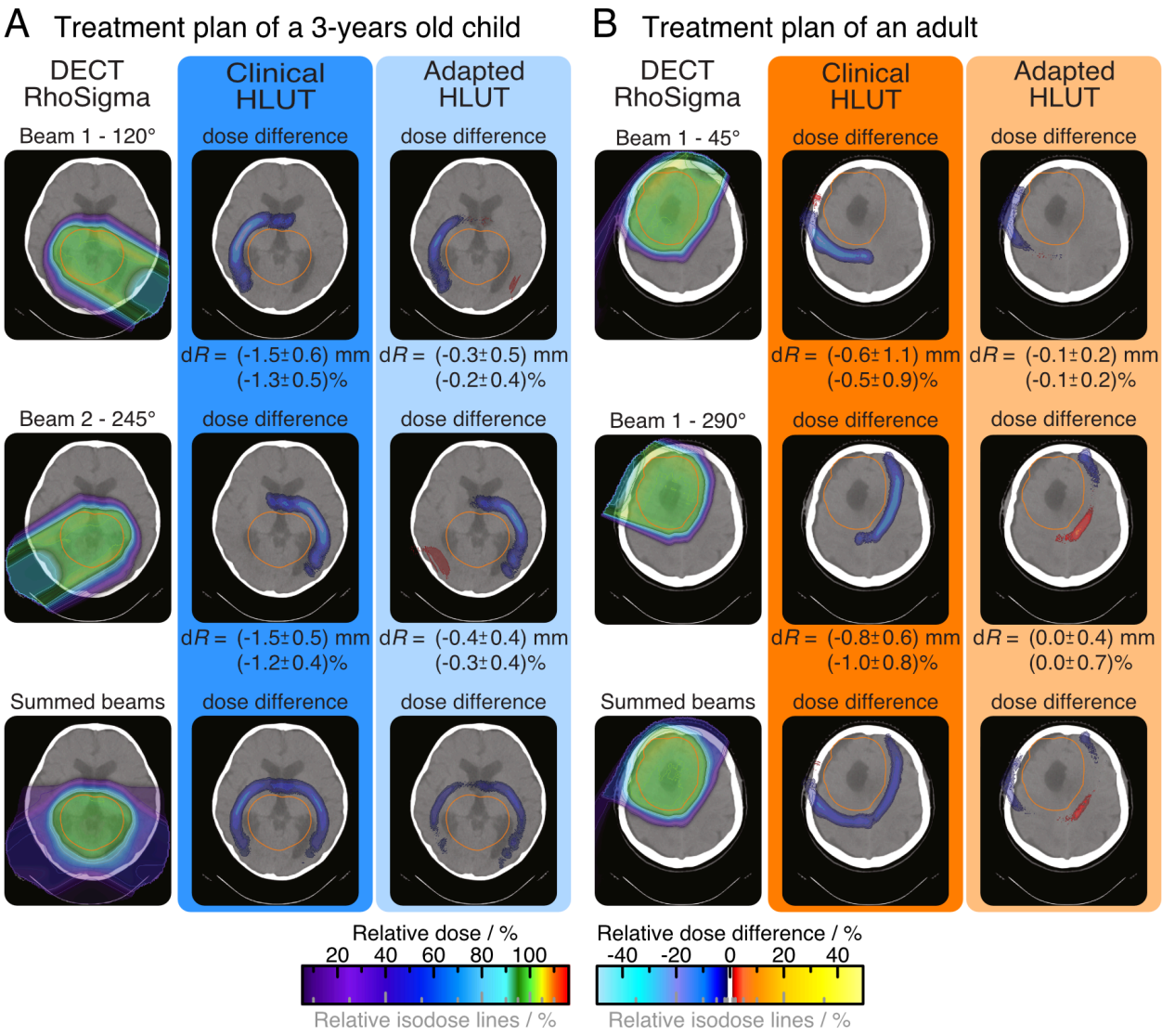

414

415 **Figure 6:** Dose difference as well as mean absolute and relative range deviation (dR) between
416 the dual-energy CT based stopping-power prediction and clinically applied or adapted
417 Hounsfield look-up table (HLUT) for two single treatment fields and the summed treatment
418 plan.

FIGURE CAPTIONS

Figure 1: Frequency distribution of tissue parameters derived from dual-energy CT for children (blue) and adults (red). The superposition of both datasets appears purple. Dashed lines illustrate correlation in bony region.

Figure 2: Age-related variation of (A) stopping-power ratio (SPR) spread in soft tissue (tissue diversity) and (B) the slope within bones (change in calcium content) for correlations between CT number and SPR. Patients were sorted in five groups depending on age (illustrated by vertical lines). Boxplots are defined according to Figure 5.

Figure 3: Frequency distribution of correlations between CT number and stopping-power ratio (SPR) for the (A) pediatric (younger than 20 years) and (B) adult patient cohort.

Figure 4: Difference in stopping-power ratio (SPR) between the dual-energy CT based SPR prediction (RhoSigma) and (A) clinically applied or (B) cohort-specifically adapted Hounsfield look-up table (HLUT) to visually compare the frequency distribution in one patient with the entire patient cohort. The colored (grey-shaded) frequency distribution covers all correlations with a frequency larger (lower) than 10^{-3}%.

Figure 5: Global and tissue-specific mean (A) signed and (B) absolute SPR deviation between the dual-energy CT based SPR prediction and clinically applied or adapted Hounsfield look-up table (HLUT). The relative amount is quoted for each tissue type below.

Figure 6: Dose difference as well as mean absolute and relative range deviation (dR) between the dual-energy CT based stopping-power prediction and clinically applied or adapted

445 Hounsfield look-up table (HLUT) for two single treatment fields and the summed treatment
446 plan.